

# An Envelope Disrupted by a Quadrupolar Outflow in the Pre-Planetary Nebula IRAS19475+3119

Ming-Chien Hsu<sup>1,2</sup> and Chin-Fei Lee<sup>1</sup>

## ABSTRACT

IRAS 19475+3119 is a quadrupolar pre-planetary nebula (PPN), with two bipolar lobes, one in the east-west (E-W) direction and one in the southeast-northwest (SE-NW) direction. We have observed it in CO J=2-1 with the Sub-millimeter Array at  $\sim 1''$  resolution. The E-W bipolar lobe is known to trace a bipolar outflow and it is detected at high velocity. The SE-NW bipolar lobe appears at low velocity, and could trace a bipolar outflow moving in the plane of the sky. Two compact clumps are seen at low velocity around the common waist of the two bipolar lobes, spatially coincident with the two emission peaks in the NIR, tracing dense envelope material. They are found to trace the two limb-brightened edges of a slowly expanding torus-like circumstellar envelope produced in the late AGB phase. This torus-like envelope originally could be either a torus or a spherical shell, and it appears as it is now because of the two pairs of cavities along the two bipolar lobes. Thus, the envelope appears to be disrupted by the two bipolar outflows in the PPN phase.

*Subject headings:* circumstellar matter – planetary nebulae: general – stars: AGB and post-AGB – stars: individual (IRAS 19475+3119): mass loss – stars:winds, outflows

## 1. Introduction

Pre-planetary nebulae (PPNe) are objects in a transient phase between the asymptotic giant branch (AGB) phase and the planetary nebula (PN) phase in the stellar evolution of a sun-like star. The PPN phase is short with a lifetime of up to thousands of years; yet it closes the gap between the two morphologically very different phases - the AGB phase and

---

<sup>1</sup>Academia Sinica Institute of Astronomy and Astrophysics, P.O. Box 23-141, Taipei 106, Taiwan; mchsu@asiaa.sinica.edu.tw, cflee@asiaa.sinica.edu.tw

<sup>2</sup>Department of Physics, National Taiwan University, Taipei 10617, Taiwan

the PN phase. The former exhibits roughly spherical AGB circumstellar envelopes (CSEs) expanding radially at 10–20 km s<sup>-1</sup>, comparable to the escape velocity of the AGB stars. Yet the latter exhibits diverse morphologies, with a significant fraction having highly collimated fast-moving bipolar or multipolar (including quadrupolar) outflow lobes (Balick & Frank 2002; Sahai 2004). In the past decades, high spatial resolution imagings of PPNe exhibit an even richer array of shapes, including multiaxial symmetries (Balick & Frank 2002), suggesting that the aspherical symmetry in the PN phase must have started in the PPN phase (Sahai 2004). It seems that collimated fast winds or jets are required to shape the PPNe and young PNe (Sahai & Trauger 1998; Soker & Rappaport 2000; Lee & Sahai 2003; Soker 2004; Sahai 2004). In particular, the departure from the spherical symmetry could result from an interaction of the jets with the preexisting AGB CSEs. Also, multipolar and/or point-symmetric morphologies could result from multiple ejections and/or change in ejection directions of the jets, respectively (Sahai et al. 2007, hereafter SSMC07).

PPNe and PNe are often seen with a dense equatorial waist structure that is often called a torus (e.g., Kwok et al. 1998; Su et al. 1998; Volk et al. 2007; Sahai et al. 2008). The origin of the torus is unknown, and it may be due to either an equatorially enhanced mass loss in the late AGB phase or an interaction between an underlying jet and the spherical AGB wind (Soker & Rappaport 2000). Tori are common in bipolar PPNe, but less common in multipolar PPNe. It is thus important to study how a torus can be formed in multipolar PPNe and its relation with the jet.

The PPN IRAS 19475+3119 is a quadrupolar nebula with two collimated bipolar lobes, one in the east-west (E-W) direction and one in the southeast-northwest (SE-NW) direction (SSMC07). In the optical image of the Hubble Space Telescope (HST), the bipolar lobes appear limb-brightened, suggesting that they are dense-walled structures with tenuous interiors or cavities (SSMC07), and that they trace two bipolar outflows produced by two bipolar post-AGB winds (Sánchez-Contreras et al. 2006, hereafter SC06; SSMC07). Its central star, HD 331319, is an F3 Ib ( $T_{eff} \sim 7200\text{K}$ ) supergiant star classified as a post-AGB object based on the elemental abundance analysis (Klochkova et al. 2002). The distance is  $\sim 4.9$  kpc by assuming a total luminosity of 8300  $L_{\odot}$ , appropriate for a post-AGB star with a mass of 0.63  $M_{\odot}$  (Hrivnak & Bieging 2005). Using this luminosity and the effective temperature, the central star is estimated to have a radius of 58  $R_{\odot}$ . This PPN has a detached circumstellar envelope based on its double-peaked spectral energy distribution (Hrivnak et al. 1999). Near-infrared (NIR) images of this PPN show a nebula extending in the SE-NW direction and a puzzling two-armed spiral-like structure (Gledhill et al. 2001). The NIR nebula is the counterpart of the SE-NW bipolar lobe in the optical. The spiral-like structure is point-symmetric and could result from an interaction of the mass-losing star with a binary companion (Gledhill et al. 2001).

Single-dish CO spectra toward this PPN show two components, a strong line core from the circumstellar envelope and weak wings from fast moving gas (Likkell et al. 1991; Hrivnak & Bieging 2005). At  $\sim 2''$  resolution, the two components are seen in CO J=2-1 as a slowly expanding shell and a fast bipolar outflow that is aligned with the E-W bipolar lobe in the optical (SC06). At  $\sim 0''.6$  resolution, a ring-like envelope is seen mainly around the E-W bipolar lobe (Castro-Carrizo et al. 2010, hereafter CC10). Here we present an observation at  $\sim 1''$  resolution in CO J=2-1 for this PPN. Our observation shows an expanding torus-like envelope around the common waist of the two bipolar lobes and that the structure and kinematics of the envelope are consistent with the envelope being disrupted by the quadrupolar nebula, or the two bipolar outflows.

## 2. Observations

Interferometric observation of IRAS 19475+3119 in CO J=2-1 was carried out using the Submillimeter Array (SMA) (Ho et al. 2004) in the extended configuration on 2009 August 29. Seven antennas were used with baselines ranging from 44 to 226 m. The SMA correlators were set up to have a channel spacing of 0.2 MHz ( $\sim 0.26 \text{ km s}^{-1}$ ) for CO J=2-1. The total duration of the observation (including the integration time on the source and calibrators) was  $\sim 11.5$  hr with a useful duration of  $\sim 5.5$  hr on the source.

The calibration of the data was performed using the MIR software package. Passband and flux calibrators were 3C84 and Uranus, respectively. The gain calibration was done with the quasar 2015+371, whose flux was estimated to be 3.05 Jy at 230 GHz, about 20% higher than that reported from the light curve measurements of the SMA around the same period of time. Each integration cycle includes 4 minutes on 2015+371 and 20 minutes on the source. The calibrated visibility data were imaged with the MIRIAD package. The dirty maps that were produced from the calibrated visibility data were CLEANed, producing the CLEAN component maps. The final maps were obtained by restoring the CLEAN component maps with a synthesized (Gaussian) beam fitted to the main lobe of the dirty beam. With natural weighting, the synthesized beam has a size of  $1''.16 \times 1''.01$  at a position angle (P.A.) of  $-63^\circ$ . The rms noise levels are  $\sim 0.1 \text{ Jy beam}^{-1}$  in the CO channel maps with a channel width of  $1 \text{ km s}^{-1}$ . The velocities of the channel maps are LSR.

### 3. Results

In the following, our results are presented in comparison to the HST image of SSMC07 and the NIR image of Gledhill et al. (2001). Note that the HST image adopted in SC06 was incorrectly rotated by  $\sim 10^\circ$  clockwise. The systemic velocity in this PPN is found to be  $18.25 \pm 1 \text{ km s}^{-1}$  from our modeling in Section 4 (see also SC06). The integrated line profile of CO shows that most emission comes from within  $\pm 15 \text{ km s}^{-1}$  from the systemic velocity. Compared with previous single-dish and interferometric observations in the same emission line (SC06), our interferometric observation at high resolution filters out most of the extended emission at low velocity, allowing us to study compact structures, such as a torus and collimated outflows, around the source.

#### 3.1. A torus-like circumstellar envelope

At low velocity (within  $\pm 10 \text{ km s}^{-1}$  from the systemic velocity), the CO map (Fig. 1) shows two compact clumps on the opposite sides of the source, one to the northeast (NE) at P.A.  $\sim 15^\circ$  and one to the southwest (SW) at P.A.  $\sim 195^\circ$ , at a distance of  $\sim 1''$  (4900 AU) from the source. These two clumps can be seen in the 7 central velocity channels from 8 to  $29 \text{ km s}^{-1}$  (Fig. 2) and have also been seen at higher resolution in CC10 as well. They are seen around the common waist of the two bipolar lobes, spatially coincident with the two emission peaks in the NIR, tracing the dense envelope around the source. The center of the two clumps, however, is shifted by  $0''.15$  to the east of the reported source position, which is  $\alpha_{(2000)} = 19^{\text{h}}49^{\text{m}}29^{\text{s}}.56$ ,  $\delta_{(2000)} = +31^\circ 27' 16''.22$  (Hog et al. 1998). This position shift is only  $\sim 15\%$  of the synthesized beam and thus can be due to the position uncertainty in our map. Also, there could be uncertainty in the reported source position. Therefore, in this paper, the center of the two clumps is considered as the source position. Faint protrusions are also seen along the two bipolar lobes at low velocity, extending to the east and west, as well as to the southeast and northwest. These faint protrusions are most likely to be from the quadrupolar lobes, and thus unlikely to be from the dense envelope itself.

The structure and kinematics of the two clumps can be studied with position-velocity (PV) diagrams cut along four different P.A., from the one aligned with their peaks (cut A with P.A. =  $15^\circ$ ) to the one perpendicular (cut D with P.A. =  $-75^\circ$ ), through the two in between (cut B with P.A. =  $-10^\circ$  and cut C with P.A. =  $-30^\circ$ ). The PV diagrams along these cuts shows a similar ring-like PV structure with less and less emission around the systemic velocity as we go from cut A to cut D (Figures 3a-d), indicating that the two clumps trace the two limb-brightened edges of a torus-like envelope at a small inclination angle (i.e, close to edge-on), either radially expanding or collapsing, with the equator aligned with cut A. In

addition, the torus-like envelope has a thickness with a half opening angle (i.e., subtended angle or see next section for the definition) of  $20^{\circ}$ – $45^{\circ}$ , measured from its equator. The two high-velocity ends of the ring-like PV structure are from the farside and nearside of the torus-like envelope projected to the source position. The emission there is bright, indicating that the material in the farside and nearside must be projected to the source position, and this requires the torus-like envelope to have an inclination angle smaller than its half opening angle. Figure 4 shows the spectrum integrated over a region with a diameter of  $\sim 2''.5$  around the source. It includes most of the torus-like envelope but excludes the protrusions along the two bipolar lobes. It shows a double-peaked line profile with the redshifted peak at  $\sim 28$   $\text{km s}^{-1}$  slightly brighter than the blueshifted peak at  $\sim 10$   $\text{km s}^{-1}$ . Since the temperature of the torus-like envelope is expected to drop away from the central star (Kwan & Linke 1982), the emission from the farside is expected to be brighter than that from the nearside because of the absorption in the nearside. Therefore, the redshifted peak in the line profile is from the farside and the blueshifted peak is from the nearside, implying that the torus-like envelope is expanding at  $\sim 10$   $\text{km s}^{-1}$ , in agreement with it being the circumstellar envelope produced in the AGB phase. The PV diagram cut perpendicular to the equator, i.e., cut along P.A.= $-75^{\circ}$ , shows that the redshifted emission shifts to the west and the blueshifted emission shifts to the east at low velocity (Fig. 3d). For an expanding torus, this indicates that the torus is inclined, with the nearside tilted to the east.

### 3.2. Outflows

At high velocity (beyond  $\pm 13$   $\text{km s}^{-1}$  from the systemic velocity), CO emission is seen around the E-W bipolar lobe seen in the optical, emerging from the two opposite poles (or holes) of the torus-like envelope (Fig. 1). This E-W bipolar lobe is already known to trace a fast-moving bipolar outflow (SC06). The PV diagram (Fig. 3e) along the outflow axis (P.A.= $88^{\circ}$ ; cut E in Fig. 1a) shows that the outflow velocity increases from the base to the tip at  $\sim 4''$  ( $\sim 20000$  AU), as found in SC06. This is why the CO emission at low-velocity is seen near the source forming the faint protrusions along the E-W bipolar lobe, as mentioned in the previous section. The radial velocities are  $\sim 30$   $\text{km s}^{-1}$  at the tip of the red-shifted lobe and  $\sim 24$   $\text{km s}^{-1}$  at the tip of the blue-shifted lobe, with a mean velocity of  $\sim 27$   $\text{km s}^{-1}$ .

The PV diagram also shows a hint of bifurcation in velocity along the outflow axis, especially for the red-shifted lobe in the east [see the dark lines in Figure 3e and also Figure 20 in CC10]. This suggests that the outflow lobe is a hollow, shell-like cavity wall, as suggested in SSMC07. For example, in the case of the redshifted lobe, the emission with

less red-shifted velocity is from the front wall, while the emission with the more red-shifted velocity is from the back wall. The outflow has the shell-like structure, likely resulting from an interaction of a post-AGB wind with the pre-existing circumstellar medium, as proposed in SC06 and SSMC07.

On the other hand, no CO emission is seen here at high velocity around the SE-NW optical bipolar lobe. It has been argued that this bipolar lobe, like the E-W bipolar lobe, is also a dense-walled structure with tenuous interiors (or cavities) (SSMC07) and could also be produced by a bipolar post-AGB wind (SC06; SSMC07). Thus, this bipolar lobe could trace a bipolar outflow moving along the plane of the sky, with the CO emission seen only at low velocity (within  $\pm 10 \text{ km s}^{-1}$  from the systemic as seen in the channel maps) forming the faint protrusions along the SE-NW bipolar lobe, as mentioned in the previous section. The low inclination is also consistent with the fact that the SE and NW components of the SE-NW bipolar lobe have almost the same brightness in the optical.

#### 4. Modeling the torus-like envelope

As discussed, the two CO clumps seen at low velocity arise from a torus-like envelope at a small inclination angle, with the nearside tilted to the east. In this section, we derive the physical properties, including the kinematics, structure, density and temperature distributions, of this torus-like envelope through modeling the two CO clumps with a radiative transfer code. The envelope appears torus-like around the common waist of the two bipolar lobes, and it could arise from a torus with or without the cavities (or holes) cleared by the bipolar lobes, or a spherical shell with the cavities. For a torus and a spherical shell, the number density of the molecular hydrogen in spherical coordinates  $(r, \theta, \phi)$  can be assumed to be

$$n = n_0 \left( \frac{r}{r_0} \right)^{-2} \cos^p \theta, \quad (1)$$

where  $\theta$  is measured from the equatorial plane of the envelope. Here  $p = 0$  for a spherical shell and  $p > 0$  for a torus with a half opening angle  $\theta_0$  defined as

$$\cos^p \theta_0 = 0.5 \quad (2)$$

Also  $r_0 = 1''$ , which is the representative radius of the torus-like envelope. The envelope has an inner radius  $R_{\text{in}}$  and an outer radius  $R_{\text{out}}$ . It is expanding radially at a velocity of  $v_e$ , and thus the mass-loss rate (including helium) can be given by

$$\dot{M} = 1.4m_{\text{H}_2} \int nv_e r^2 d\Omega = 2.8\pi m_{\text{H}_2} n_0 v_e r_0^2 \int \cos^p \theta d\theta \quad (3)$$

The cavities, if needed, are assumed to have a half-ellipsoidal (like paraboloidal) opening for simplicity, with the semi-major axis and semi-minor axis determined from the bipolar lobes in the optical. Inside the cavities, the number density of the envelope is set to zero.

In the envelope, the temperature profile is assumed to be

$$T = T_0 \left( \frac{r}{r_0} \right)^{-1} \quad (4)$$

similar to that derived by Kwan & Linke (1982) for AGB envelopes, including gas-dust collisional heating, adiabatic cooling, and molecular cooling.

In our models, radiative transfer is used to calculate the CO emission, with an assumption of local thermal equilibrium. The relative abundance of CO to H<sub>2</sub> is assumed to be  $4 \times 10^{-4}$ , as in SC06. For simplicity, the line width is assumed to be given by the thermal line width only. Also, the systemic velocity  $v_{\text{sys}}$  is assumed to be a free parameter. The channel maps of the emission derived from the models are used to obtain the integrated intensity map, spectrum, and PV diagrams to be compared with the observation. Note that the observed emission in the east, west, southeast, and northwest protrusions at low velocity (Fig. 1) is not from the envelope and thus will not be modeled here. In our models, the free parameters are  $v_{\text{sys}}$ ,  $v_e$ ,  $R_{\text{in}}$ ,  $R_{\text{out}}$ ,  $p$  (torus or spherical shell), cavities (holes), inclination angle  $i$ , equator PA,  $n_0$ , and  $T_0$ . Table 1 shows the best-fit parameters for our models with different structures. Our models all require  $v_{\text{sys}} \sim 18.25 \pm 1 \text{ km s}^{-1}$  and  $v_e \sim 12.5 \pm 1.5 \text{ km s}^{-1}$  to fit the two velocity ends in the PV diagrams and the spectrum. They require  $R_{\text{in}} \sim 0''.7$  (3430 AU) and  $R_{\text{out}} \sim 1''.6$  (7840 AU) to match the emission peak positions. They also require  $T_0$  to be  $\sim 28 \text{ K}$  to match the emission intensity, resulting in an overall characteristic (or mean) temperature of  $\sim 23 \text{ K}$  for the envelope. This characteristic temperature is slightly higher than the values found in the more extended envelope by SC06 and SSMC07 at lower resolutions. This is reasonable, because the envelope temperature is expected to be higher near the source. In the following, we discuss our different models in detail.

#### 4.1. A Torus without cavities

First we check if a simple torus model can reproduce the two clumps (Figure 5). In this model, the equator of the torus is set to be at P.A.=15°, to be aligned with the two clumps. As expected, the torus is required to have a small inclination angle of  $\sim 15^\circ$  and a small half opening angle of  $\theta_0 \sim 24^\circ$  with  $p = 8$ . This model can reproduce reasonably well the compactness of the two clumps. It can also reproduce the ring-like PV structures, and the less and less emission around the systemic velocity in the PV diagrams from cut A to cut D. Note that the PV diagram cut along the equatorial plane shows a ring-like structure



with two C-shaped peaks at the two high velocity ends facing to each other, because the emission is symmetric about the equatorial plane. For the PV diagrams with a cut away from the equatorial plane, the blueshifted emission shifts to the southeast and the redshifted emission shifts to the northwest, because the torus is inclined with the nearside tilted to the southeast. For the spectrum, the model can produce the double-peaked line profile, however, it produces higher intensity than the observed around the systemic velocity (Fig. 5b).

#### 4.2. A Torus with a E-W pair of cavities

Here we add a E-W pair of cavities to the above simple torus model and see if we can reproduce the spectrum better by reducing the intensity around the systemic velocity (Figure 6). The E-W pair of cavities are assumed to have a half-ellipsoidal opening with a semi-major axis of  $2''$  and a semi-minor axis of  $1''$ , as measured from the HST image (Fig. 1). The E-W pair of cavities have a P.A.= $88^\circ$  and can have an inclination angle from  $10^\circ$  to  $30^\circ$ , with the western cavity titled toward us, as suggested in SC06. These moderate inclinations are consistent with the optical image that shows the eastern lobe is slightly fainter than the western lobe, and they all give similar results in our model. The model results here are similar to those of the simple torus model above, with some slight differences. This is because the E-W pair of cavities are almost aligned with the poles of the torus, and removing the tenuous material in the poles does not change much the model results. The cavities remove slightly the blueshifted emission in the west and redshifted emission in the east, mainly at low velocity, as seen in the spectrum. In addition, unlike that in the torus model, the PV diagram cut along the equatorial plane shows a ring-like structure with two sickle-shaped peaks, instead of two C-shaped peaks, at the two high velocity ends facing to each other (comparing Figure 5c and Figure 6c). This is because that, along that cut direction, the E-W pair of cavities remove the redshifted material in the north, and blueshifted emission in the south.

#### 4.3. A Torus with 2 pairs of cavities

Here we add one more pair of cavities, the SE-NW pair, into our model (Figure 7). Again, this pair of cavities are assumed to have a half-ellipsoidal opening but with a semi-major axis of  $2''$  and a semi-minor axis of  $0''8$ , as measured from the HST image (Fig. 1). This pair of cavities have a P.A.= $-40^\circ$  and are assumed to have an inclination of  $0^\circ$  (i.e., in the plane of the sky). Adding this pair of cavities will rotate the two clumps counterclockwise about the source. Therefore, the torus in this model is required to have its equator at a



smaller P.A. of  $10^\circ$  in order for the two clumps to appear at P.A.= $15^\circ$ . As a result, the underlying torus could be initially more perpendicular to the E-W bipolar lobe. Also, a higher density is required to reproduce the same amount of flux in the clumps (see Table 1).

By removing the material along the SE-NW bipolar lobe, this model can now reproduce the required dip around the systemic velocity in the double-peaked spectrum. This is because that the SE-NW pair of cavities, being in the plane of the sky, remove the low-velocity emission preferentially. This model can also reproduce the ring-like PV structures, and the less and less emission around the systemic velocity in the PV diagrams from cut A to cut D. Note that, in the PV diagram cut along the equatorial plane, the model shows two sickle-shaped peaks, which could be somewhat different from the observation in detail. This detailed difference could be due to localized excitation effect near the base of the E-W cavities and should not affect our main conclusions on the envelope properties.

#### 4.4. A Spherical shell with 2 pairs of cavities

A spherical shell with only the E-W pair of cavities can be ruled out because it would produce two clumps that are exactly perpendicular to the E-W bipolar lobe, inconsistent with the observation. Therefore, here we check if a spherical shell with the same 2 pairs of cavities as above can produce the two clumps in the observation. We find that this model is quite similar to the torus model with the 2 pairs of cavities, except that the two clumps are slightly rotated and the emission is more extended perpendicular to the torus-like structure, in between the cavities (comparing Figure 8a to Figure 7a). This slight rotation is acceptable because our model is simple and the two clumps are not resolved in our observation. On the other hand, further observation that can separate the envelope from the two bipolar lobes is needed to check if the emission extending perpendicular to the torus-like structure in this model is inconsistent with the observation.

#### 4.5. Model summary

Our model results show that the two CO clumps could arise from either a torus or a spherical shell, with two pairs of cavities, one along the E-W bipolar lobe and one along the SE-NW bipolar lobe. A pure torus model and a torus with only a E-W pair of cavities both produce more than observed emission around the systemic velocity in the spectrum. In addition, the SE-NW pair of cavities, being in the plane of the sky, are essential to remove the low-velocity emission in our models. All the models are optically thin. With the mean

envelope temperature of 23 K and the model brightness temperature of  $\sim 4$  K, the mean optical depth is  $\sim 0.2$ . Therefore, in the model spectra, the redshifted peak is only slightly brighter than the blueshifted peak, as observed. The mass-loss rate of the AGB wind derived from our two best models is  $\sim 2 - 3 \times 10^{-5} M_{\odot} \text{ yr}^{-1}$ . In the shell model, the mass-loss rate is about three times smaller than that derived from a similar shell model by SC06, which was found to be  $\sim 10^{-4} M_{\odot} \text{ yr}^{-1}$ . This is probably because of the following reasons: (1) our inner radius is smaller than theirs, and the emission is more efficient in the inner region where the density and temperature are both higher; (2) a large amount of missing flux in our observation; and (3) their envelope emission seen at low resolution could be significantly contaminated by the outflows. Therefore, the mass loss rate derived here could be a lower limit. Alternatively, the mass-loss rate might have decreased with time.

## 5. Discussion

### 5.1. The expanding torus-like envelope

In our observation, two clumps are seen in CO at the common waist of the two optical bipolar lobes, spatially coincident with the two peaks in the NIR polarization image (Figure 1), tracing the dense envelope material. These two clumps are also seen at higher resolution by CC10, but not spatially resolved at lower resolution in SC06. From our models, they are found to trace the two limb-brightened edges of an expanding torus-like envelope around the source, with an inclination angle of  $\sim 15^{\circ}$ . This torus-like envelope corresponds to the ring-like envelope found at higher resolution at a similar inclination angle in CC10. At a lower resolution of  $\sim 2''$ , two different clumps were seen in CO but aligned with the SE-NW optical bipolar lobe (SC06) as well as the SE-NW NIR nebula. Those clumps are also seen here but appear as the two faint protrusions along the SE-NW bipolar lobe (Fig.1a). As mentioned before, the two optical bipolar lobes, both E-W and SE-NW, have been found to be dense-walled structures with tenuous interiors (i.e., cavities) (SSMC07) and these cavities are indeed required in our models. Thus, our protrusions or their clumps along the SE-NW bipolar lobe likely trace the unresolved dense wall materials (i.e., swept-up material) of that bipolar lobe as suggested in SC06 and SSMC07. They only appear at low velocity likely because the SE-NW bipolar lobe is lying in the plane of the sky, as supported by the similar brightness of the SE and NW components of the bipolar lobe, in both the HST optical and the NIR images. They are faint here in our CO observation probably because their CO emission merges with that of the extended circumstellar envelope and halo, and is thus mostly resolved out. Two other protrusions are also seen at low velocity along the E-W bipolar lobe (Fig. 1a), tracing the unresolved dense wall materials of the bipolar lobe.

## 5.2. The shaping mechanism and its consequences

The PPN 19475+3119 is not spherically symmetric, with a torus-like envelope at the common waist of the two bipolar lobes. The torus-like envelope is expanding at a speed of  $\sim 12.5 \text{ km s}^{-1}$ , and thus has a dynamical age of  $\sim 1900 \text{ yr}$ , with a radius of  $\sim 5000 \text{ AU}$  ( $\sim 1''$ ). The E-W bipolar lobe has a mean inclination of  $\sim 20^\circ$ , so the mean deprojected velocity is  $\sim 27/\sin(20) \sim 80 \text{ km s}^{-1}$  at the tips and the mean deprojected distance of the tips is  $\sim 21000 \text{ AU}$  ( $\sim 4''3$ ). Thus, the dynamical age of the E-W bipolar lobe is estimated to be  $\sim 1200$  years ( $\pm 400$  years), more than half of that of the torus-like envelope. The SE-NW bipolar lobe is about half the length of the E-W bipolar lobe and may have a similar dynamical age to the E-W bipolar lobe within a factor of two. The bipolar lobes and torus-like envelope are believed to be physically related. The envelope is believed to be the AGB envelope formed by the late AGB wind. The two bipolar lobes could trace two bipolar outflows produced by two distinct bipolar post-AGB winds ejected in two different directions, as proposed in SC06 and SSMC07. The denser-wall structures with tenuous interiors (cavities) of the bipolar lobes could result from the interactions between the post-AGB winds and the envelope as shown in hydrodynamical simulations (Lee & Sahai 2003; Lee, Hsu, & Sahai 2009). Also, according to our models, the envelope, originally either a torus or a spherical shell, is disrupted by the two bipolar lobes or outflows, and it appears as it is now because of the disruptive interactions.

Could the torus-like envelope originally be a torus, like the dense equatorial waist structure often seen in other PPNe (Volk et al. 2007; Sahai et al. 2008)? If so, it could be due to an equatorially enhanced mass loss in the late AGB phase (see the review by Balick & Frank 2002). Such a dense waist, where large grains can grow, seems to be needed to account for the millimeter/submillimeter excess toward this source, as argued by SSMC07. This toroidal envelope may help collimate the E-W bipolar outflow in its pole direction. However, it is hard for the toroidal envelope to collimate two bipolar outflows that are almost perpendicular to each other, such as those in this PPN. Instead, the envelope appears to be disrupted by the two outflows, as discussed above.

On the other hand, could the torus-like envelope be a remnant of a spherical AGB shell in the inner part? The torus-like envelope has an expansion velocity similar to that of the surrounding halo (SSMC07), and thus may have the same origin as the halo, which is the spherical circumstellar shell formed by an isotropic AGB wind in the past. As discussed before, a spherical shell model with 2 pairs of cavities along the two bipolar lobes can produce a torus-like envelope as observed. Thus, the torus-like envelope could indeed be the remnant of the AGB shell in the inner part. Note that SC06 have also tried a similar spherical shell model but only with a pair of cavities along the E-W bipolar lobe. As mentioned in Section 4.4, however, this model would produce two clumps that are perpendicular to the

E-W bipolar lobe, but not at the common waist of the two bipolar lobes as observed. A similar model with 2 pairs of cavities has been adopted to explain the clumpy hollow shell morphology of the Egg Nebula by Dinh-V-Trung & Lim (2009). In that PPN, the spherical AGB envelope is also disrupted by the outflows. In this PPN, the spherical shell is disrupted more dramatically, leaving behind a torus-like envelope.

The envelope, originally either a torus or a spherical shell, will not be able to collimate the two bipolar outflows, as discussed. Therefore, the two collimated outflows in this PPN must be produced by two post-AGB winds that are intrinsically collimated or jets, as proposed in other PPNe and young PNe (Sahai & Trauger 1998; Sahai 2001; Lee & Sahai 2003; SC06). One popular model to produce a collimated jet requires a binary companion to accrete the material from the AGB star and then launch the jet (see the review by Balick & Frank 2002). Gledhill et al. (2001) also suggested that a binary interaction is needed to produce the two-armed spiral structure seen in the NIR polarization image of this PPN. The binary interaction can also transform the isotropic mass loss of the AGB wind into an equatorial enhanced mass loss (Mastrodemos & Morris 1998), producing a toroidal envelope as needed in our model. However, it is unclear how two jets can be launched in this PPN to produce the two bipolar outflows (see SSMC07, for various possibilities).

## 6. Conclusions

IRAS 19475+3119 is a quadrupolar PPN, with two bipolar lobes, one in the east-west (E-W) direction and one in the southeast-northwest (SE-NW) direction. The E-W bipolar lobe is known to trace a bipolar outflow and it is detected at high velocity. The SE-NW bipolar lobe appears at low velocity, and could trace a bipolar outflow moving in the plane of the sky. Two compact clumps are seen at low velocity around the common waist of the two bipolar lobes, spatially coincident with the two emission peaks in the NIR, tracing dense envelope material. They are found to trace the two limb-brightened edges of a torus-like circumstellar envelope, expanding away at  $\sim 12.5 \text{ km s}^{-1}$ . This torus-like envelope can be reproduced reasonably well with either a torus or a spherical shell, both with two pairs of cavities along the two bipolar lobes. Here, the torus could come from an equatorial enhanced mass loss and the spherical shell could come from an isotropic mass loss, both in the late AGB phase. In either case, the circumstellar envelope appears to be disrupted by the two bipolar outflows.

We thank the referee for the valuable comments. M.-C. Hsu appreciates valuable discussion with Chun-Hui Yang, especially in the development of the radiative transfer code. C.-F.

Lee and M.-C. Hsu are financially supported by the NSC grant NSC96-2112-M-001-014-MY3.

## REFERENCES

- Balick, B., & Frank, A. 2002, *ARA&A*, 40, 439
- Castro-Carrizo, A., et al. 2010, *A&A*, 523, A59 (CC10)
- Dinh-V-Trung, & Lim, J. 2009, *ApJ*, 698, 439
- Gledhill, T. M., Chrysostomou, A., Hough, J. H., & Yates, J. A. 2001, *MNRAS*, 322, 321
- Ho, P. T. P., Moran, J. M., & Lo, K. Y. 2004, *ApJ*, 616, L1
- Hog, E., Kuzmin, A., Bastian, U., Fabricius, C., Kuimov, K., Lindegren, L., Makarov, V. V., & Roeser, S. 1998, *A&A*, 335, L65
- Hrivnak, B. J., Langill, P. P., Su, K. Y. L., & Kwok, S. 1999, *ApJ*, 513, 421
- Hrivnak, B. J., & Bieging, J. H. 2005, *ApJ*, 624, 331
- Klochkova, V. G., Panchuk, V. E., & Tavalzhanskaya, N. S. 2002, *Astronomy Letters*, 28, 49
- Kwan, J., & Linke, R. A. 1982, *ApJ*, 254, 587
- Kwok, S., Su, K. Y. L., & Hrivnak, B. J. 1998, *ApJ*, 501, L117
- Lee, C.-F., & Sahai, R. 2003, *ApJ*, 586, 319
- Lee, C.-F., Hsu, M.-C., & Sahai, R., 2009, *ApJ*, 696, 1630
- Likkell, L., Forveille, T., Omont, A., & Morris, M. 1991, *A&A*, 246, 153
- Mastrodemos, N., & Morris, M. 1998, *ApJ*, 497, 303
- Sahai, R., 2001, in *Post-AGB Objects as a Phase of Stellar Evolution*, ed. R. Szczerba & S. K. Górný (Dordrecht: Kluwer), 53
- Sahai, R. 2004, *Asymmetrical Planetary Nebulae III: Winds, Structure and the Thunderbird*, 313, 141
- Sahai, R., Sánchez Contreras, C., Morris, M., & Claussen, M. 2007, *ApJ*, 658, 410 (SSMC07)
- Sahai, R., & Trauger, J. T. 1998, *AJ*, 116, 1357

Sahai, R., Young, K., Patel, N., Sánchez Contreras, C., & Morris, M. 2008, *Ap&SS*, 313, 241

Sánchez Contreras, C., Bujarrabal, V., Castro-Carrizo, A., Alcolea, J., & Sargent, A. 2006, *ApJ*, 643, 945 (SC06)

Soker, N. 2004, *Asymmetrical Planetary Nebulae III: Winds, Structure and the Thunderbird*, 313, 562

Soker, N., & Rappaport, S. 2000, *ApJ*, 538, 241

Su, K. Y. L., Volk, K., Kwok, S., & Hrivnak, B. J. 1998, *ApJ*, 508, 744

Volk, K., Kwok, S., & Hrivnak, B. J. 2007, *ApJ*, 670, 1137

Table 1. The best fit parameters for our models

Parameters	Torus no cavities	Torus + EW cavities	Torus + 2 pairs of cavities	Shell Model + 2 pairs of cavities
$p$	8	8	8	0
Inclination $i$	15	15	15	–
equator P.A.	15	15	10	–
$n_0$ (cm <sup>-3</sup> )	$7.5 \times 10^3$	$7.5 \times 10^3$	$9.0 \times 10^3$	$4.3 \times 10^3$
$T_0$ (K)	28	28	28	28
$v_e$ (km s <sup>-1</sup> )	12.5	12.5	12.5	12.5
$\dot{M}$ (M <sub>⊙</sub> yr <sup>-1</sup> )	$1.9 \times 10^{-5}$	$1.9 \times 10^{-5}$	$2.3 \times 10^{-5}$	$2.7 \times 10^{-5}$

Note. — The torus model with  $p=8$  has a half opening angle of  $\theta_0 \sim 24^\circ$ . Here the 2 pairs of cavities include the E-W pair and SE-NW pair of cavities. The E-W pair of cavities have a P.A.= $88^\circ$  and a mean inclination angle of  $\sim 20^\circ$ , with the western cavity tilted toward us. The SE-NW pair of cavities have a P.A.= $-40^\circ$  and are assumed to have an inclination of  $0^\circ$ .



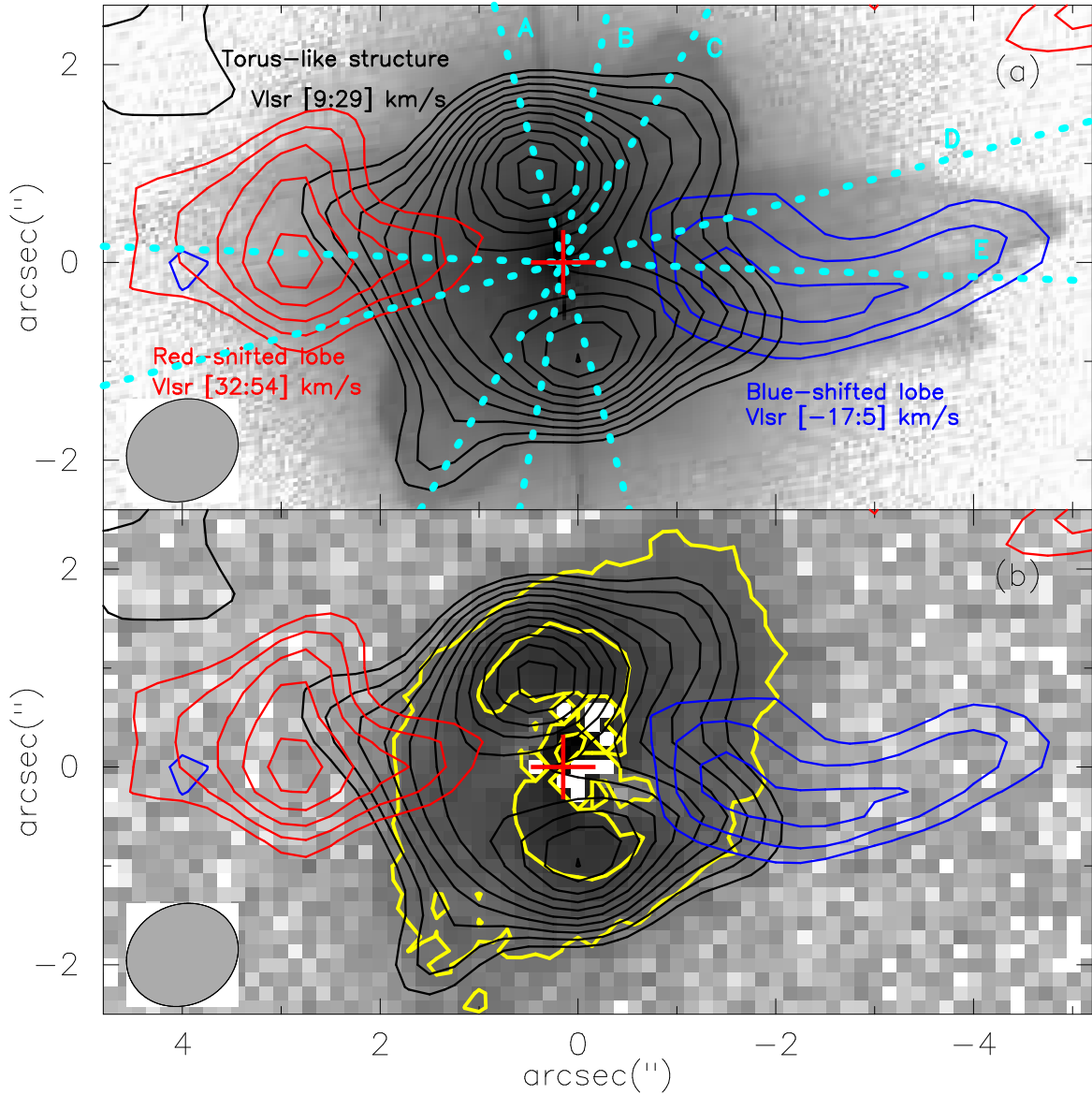


Fig. 1.— CO J=2-1 contours of IRAS 19475+3119 superposed on top of (a) the HST image obtained with F606W filter (SSMC07) and (b) the NIR image (with yellow contours, Gledhill et al. 2001). The central source position is marked by a “+”. The synthesized beam of the CO observation is shown in the left corner, with a size of  $1''.16 \times 1''.01$ . The CO intensity maps integrated over three selected LSR velocity intervals show the torus-like structure (black contours), redshifted (red contours) and blueshifted (blue contours) outflow lobes. Contour levels all start from  $2\sigma$  with a spacing of  $1\sigma$ , where  $\sigma$  is  $0.45 \text{ Jy beam}^{-1} \text{ km s}^{-1}$ . Labels A–E show the cuts for the position-velocity (PV) diagrams in Figure 3.

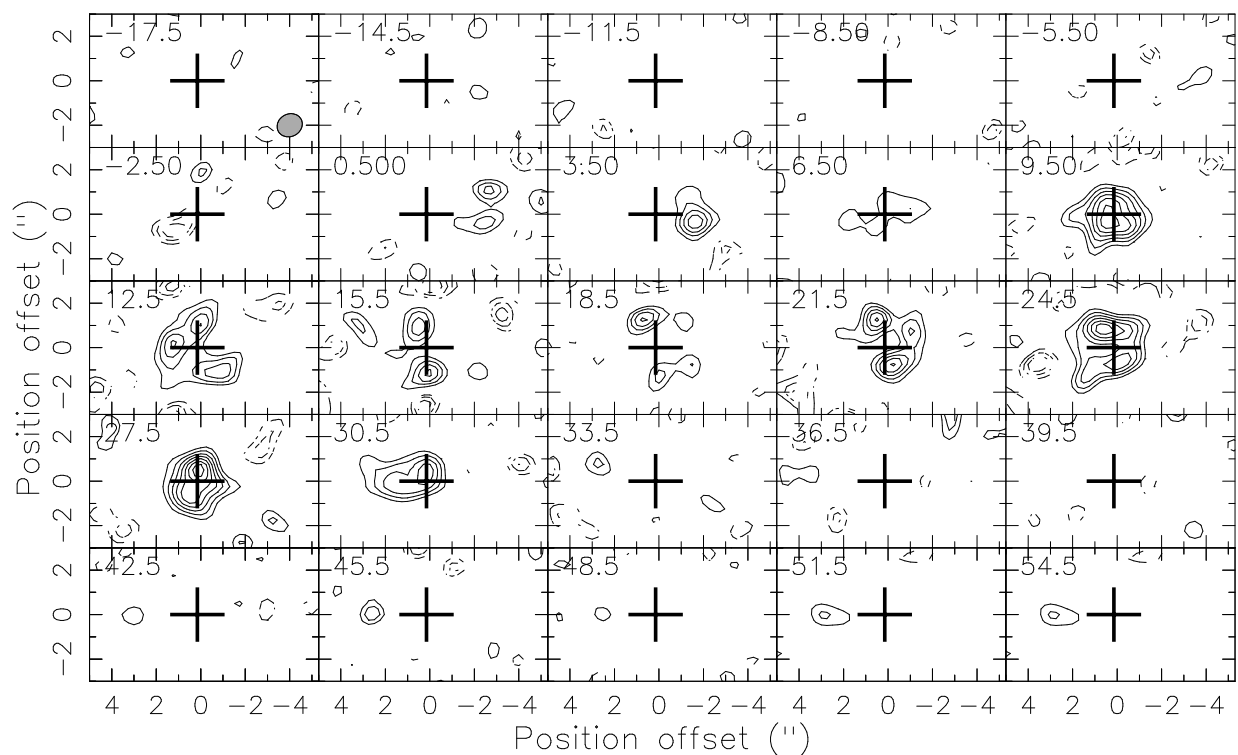


Fig. 2.— Channel maps of CO J=2-1 emission in IRAS 19475+3119. The velocity width is  $3.0 \text{ km s}^{-1}$ . The systemic velocity is  $18.25 \pm 1 \text{ km s}^{-1}$ , as found in our model. The contour levels start from  $2\sigma$  with a spacing of  $1\sigma$ , where  $\sigma = 0.06 \text{ Jy beam}^{-1}$ . The stellar position is marked by a cross. The synthesized beam is shown in the first channel map at the lower right corner. The velocity in each channel is shown in the top left corner.

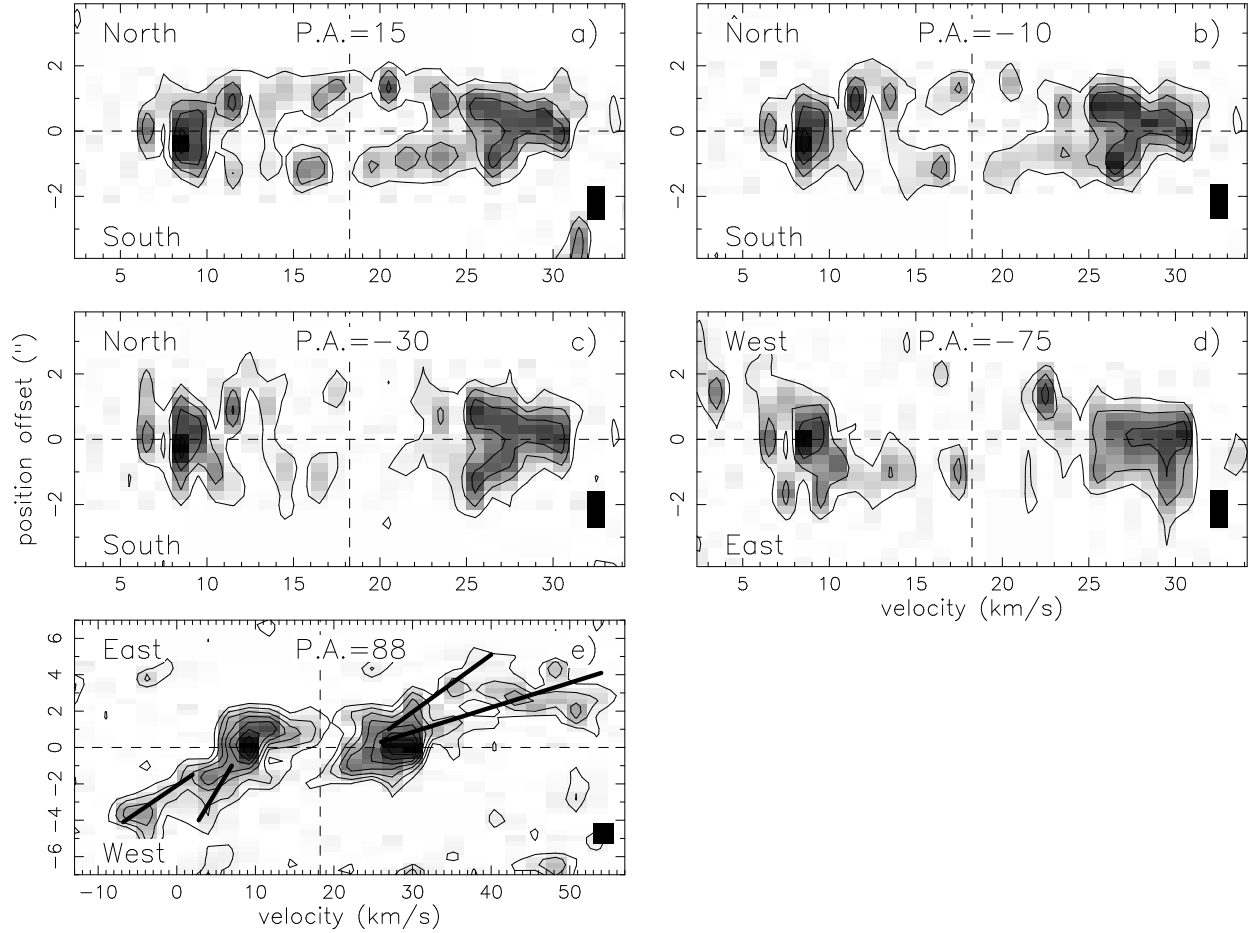


Fig. 3.— PV diagrams of the CO emission, with the cut directions shown in Figure 1a. The contour levels start from  $2\sigma$  with a spacing of  $2\sigma$ , where  $\sigma = 0.06 \text{ Jy beam}^{-1}$  in (a)-(d) and  $0.03 \text{ Jy beam}^{-1}$  in (e). The spatial and velocity resolutions are shown as a rectangle in the bottom right corner. (a) Cut A (along P.A. $=15^\circ$ ) goes through the emission peaks of the two low-velocity clumps, showing a ring-like PV structure. (b) Cut B (along P.A. $=-10^\circ$ ) goes along the axis half way to the edges of the clumps. It also shows a ring-like structure but with a weaker emission around the systemic velocity. (c) Cut C (along P.A. $=-30^\circ$ ) goes through the edges of the clumps, showing a breakup of the ring-like PV structure. (d) Cut D (along P.A. $=-75^\circ$ ) goes perpendicular to the axis connecting the two clumps, showing the emission shifted to the east on the blueshifted side and to the west on the redshifted side. (e) Cut E (along P.A. $=88^\circ$ ) goes along the high-velocity component in the east-west direction, showing a velocity increasing with the distance from the source for the outflow, and a hint of bifurcation of the PV structure (solid lines).

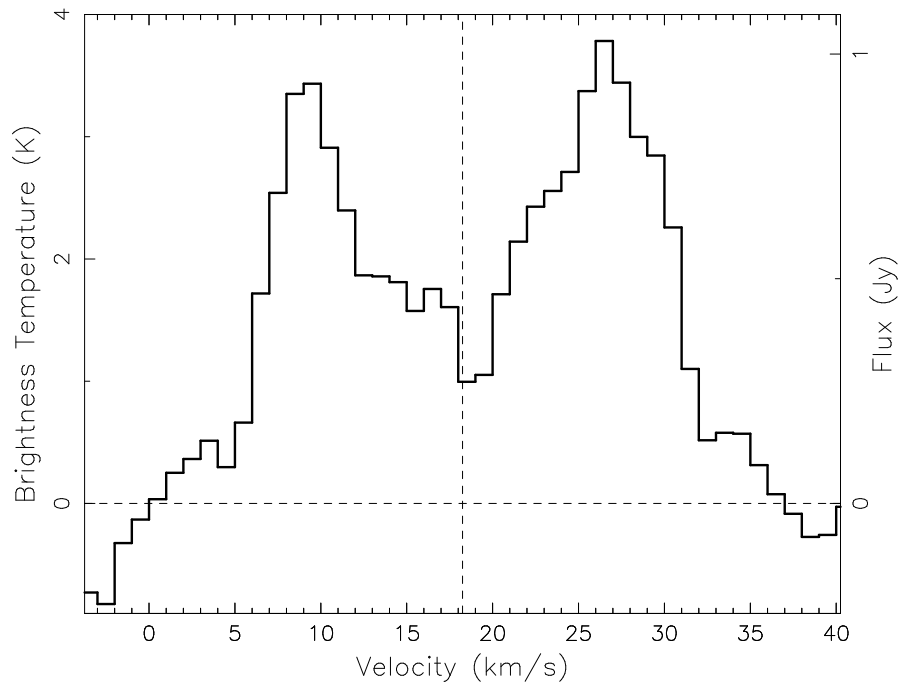


Fig. 4.— CO spectrum toward the center position, averaged over a region with a diameter of  $2''.5$ . Note that a bigger region will include emission from the two bipolar lobes. The vertical dashed line shows the systemic velocity. The spectrum shows more emission on the redshifted side than the blueshifted side, as expected for an expanding envelope.

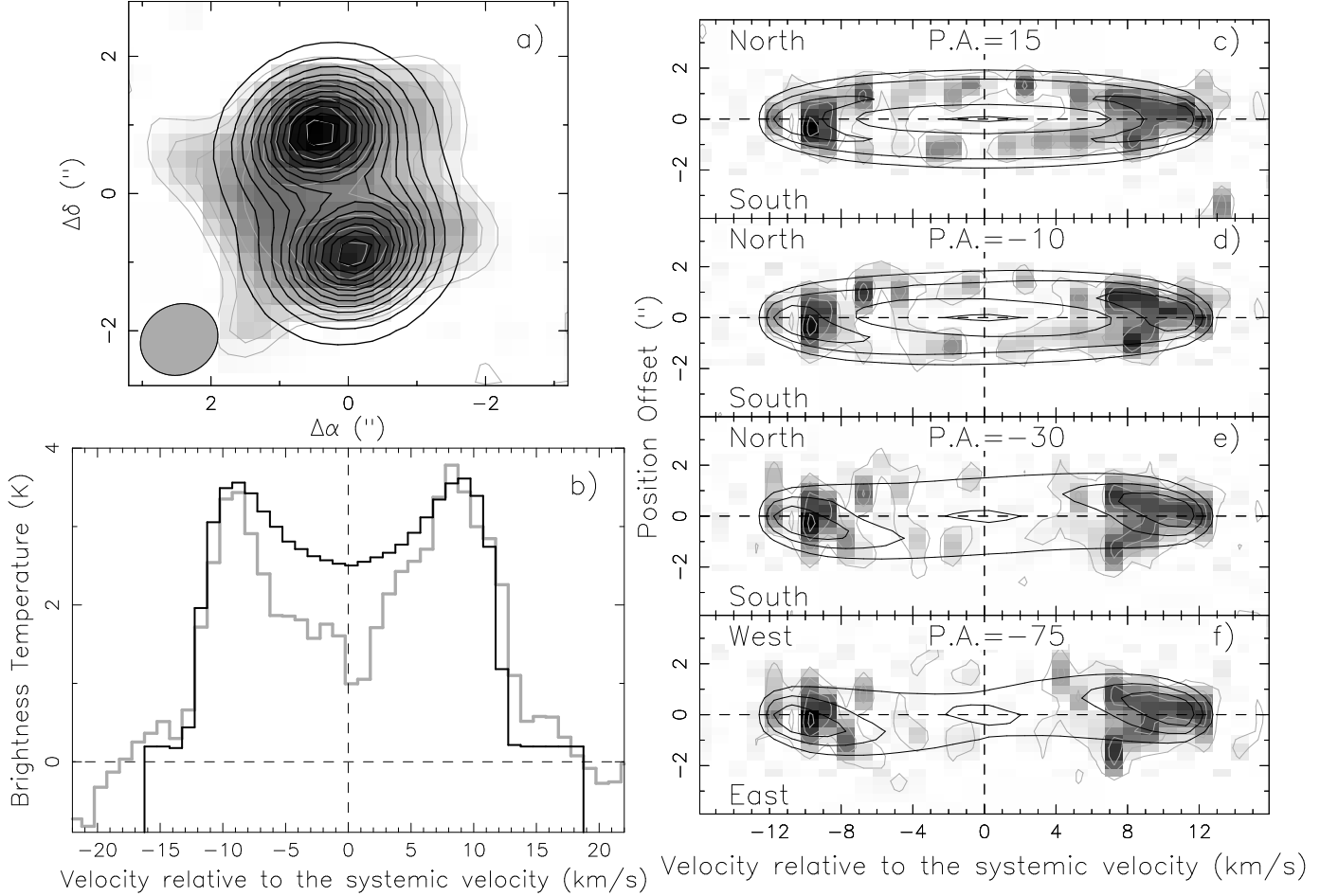


Fig. 5.— Comparison of our torus model with the observed torus-like envelope in (a) integrated intensity map as shown in Figure 1, (b) spectrum as shown in Figure 4, and (c)-(f) PV diagrams as shown in Figure 3a-d. Black contours and spectrum are from the model. The best fit model requires  $p = 8$  and an inclination of  $\sim 15^\circ$ .

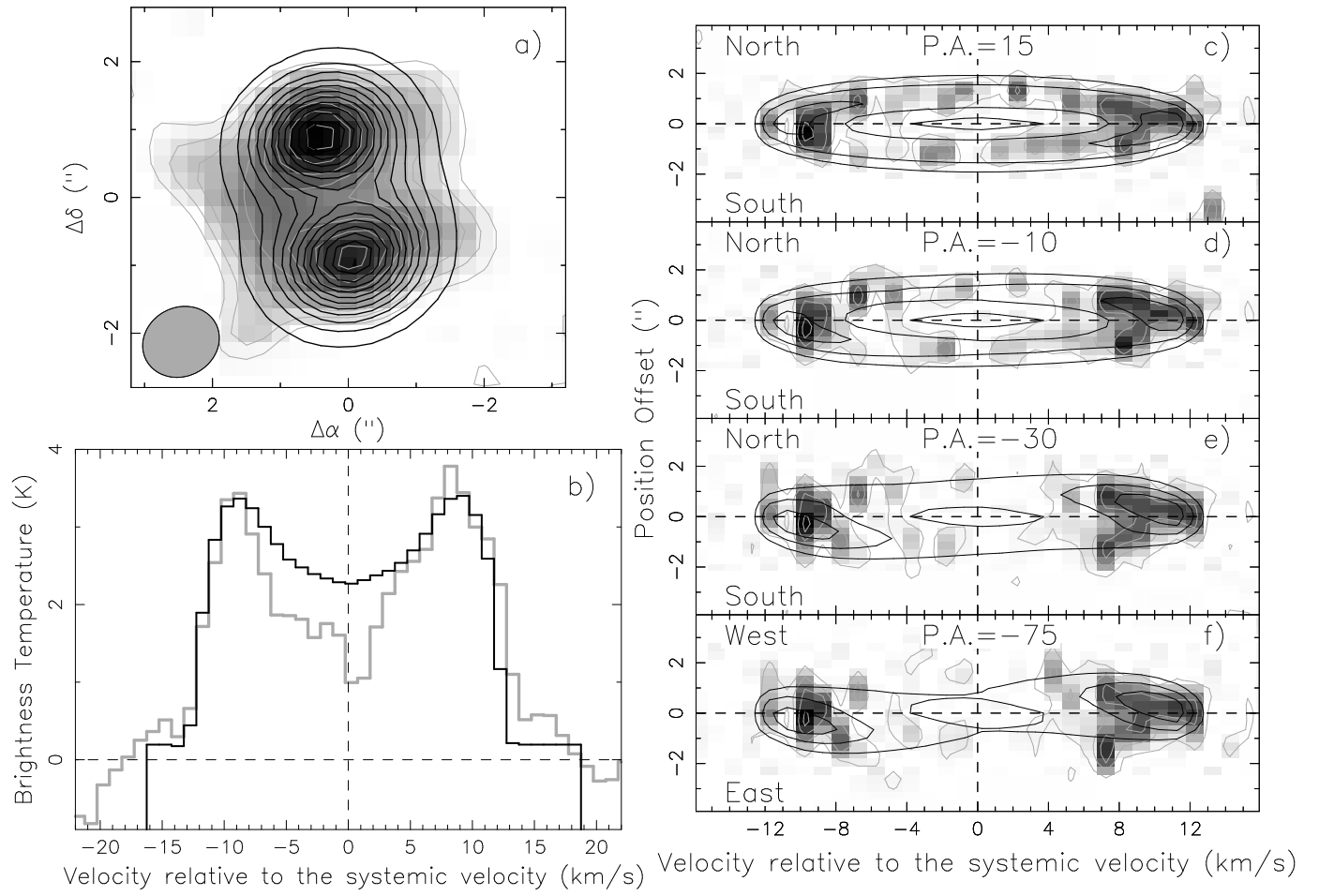


Fig. 6.— Same as Figure 5 but for the torus + EW pair of cavities model.

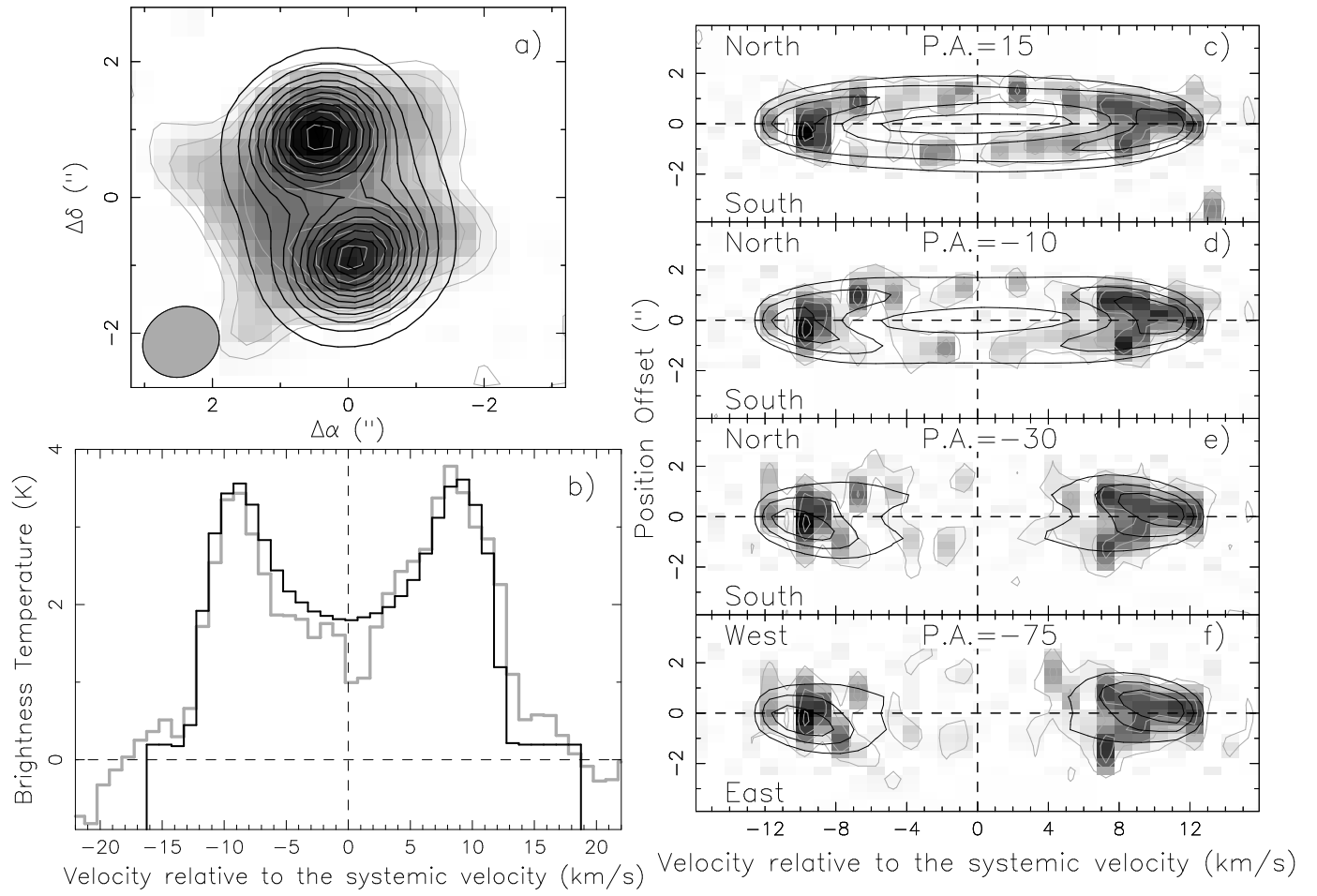


Fig. 7.— Same as Figure 5 but for the torus + 2 pairs of cavities model.



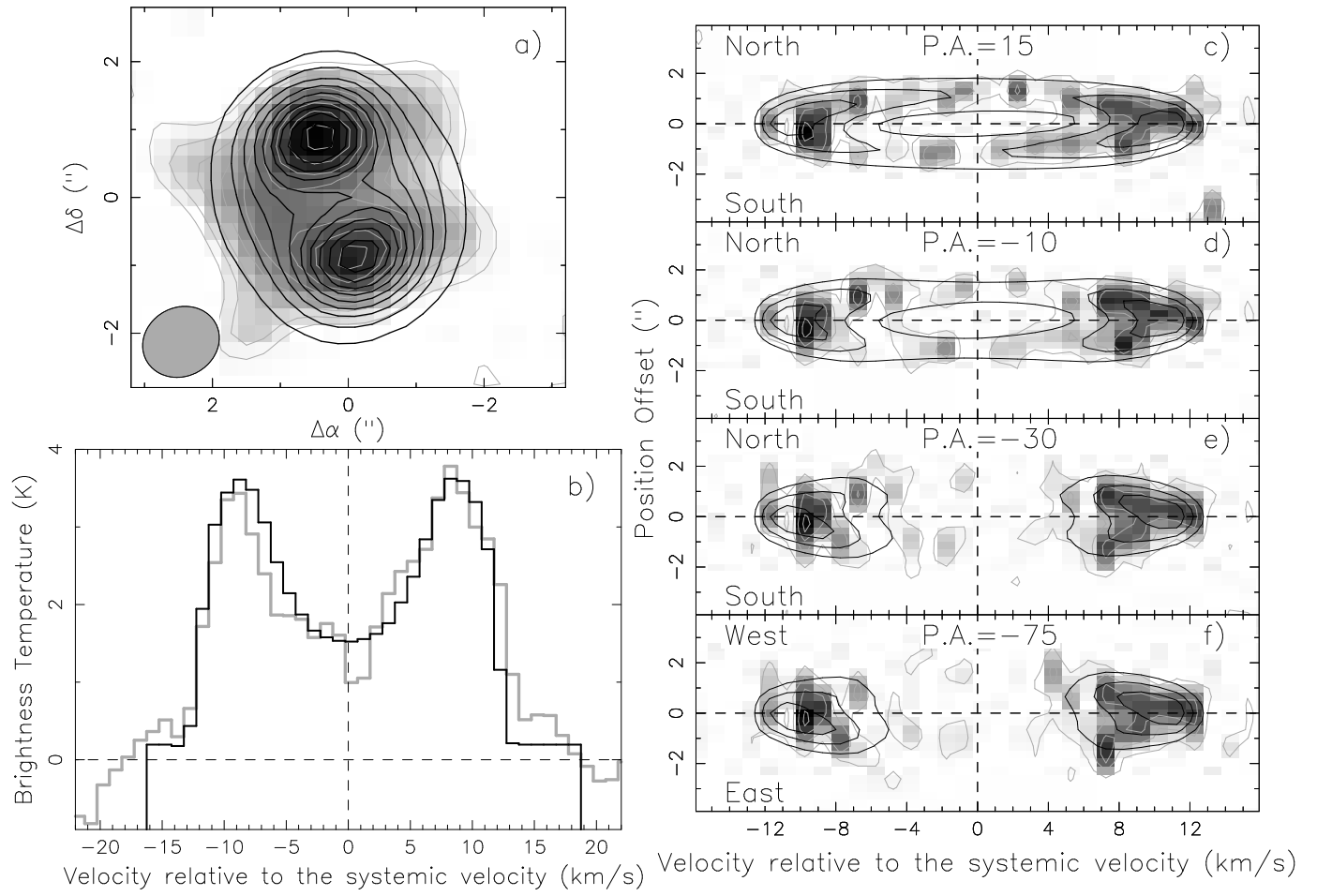


Fig. 8.— Same as Figure 5 but for the spherical shell + 2 pairs of cavities model.